

Article

An Electrochemical Impedance Spectrum-Based State of Health Differential Indicator with Reduced Sensitivity to Measurement Errors for Lithium–Ion Batteries

Jaber Abu Qahouq

Department of Electrical and Computer Engineering, College of Engineering, The University of Alabama, Tuscaloosa, AL 35487, USA; jaberq@eng.ua.edu; Tel.: +1-205-348-8669

Abstract: As the use of electrochemical batteries, especially lithium–ion (Li-Ion) batteries, increases due to emerging applications and expanding markets, the accurate and fast estimation of their state of health (SOH) is becoming increasingly important. The accuracy of the SOH estimation is highly dependent on the correlation strength between the used indicator and SOH and the accuracy of the SOH indicator measurement. This paper presents a new differential indicator which has a strong and consistent correlation with the SOH of Li-Ion batteries, based on a new Electrochemical Impedance Spectrum (EIS) Phase–Magnitude relationship. It is shown in this paper that the EIS Phase–Magnitude relationship exhibits a phase-based differential impedance magnitude SOH indicator between a first-phase peak point and a last-phase valley point. Because of the differential nature of this SOH indicator and because the two impedance values are measured at a phase peak point and a valley phase point regardless of the phase absolute values, the effect of impedance measurement shift/offset (error) on SOH estimation is reduced. This supports the future development of more accurate and faster online and offline SOH estimation algorithms and systems that have a higher immunity to impedance measurement shift/offset (error). Furthermore, in this work, the EIS was measured for a lithium–ion battery that was down to a ~15% SOH, which was not only used to support the conclusions of this paper, but also helped in filling a gap in the literature for EIS data under deep/high degradation levels.



Citation: Abu Qahouq, J. An Electrochemical Impedance Spectrum-Based State of Health Differential Indicator with Reduced Sensitivity to Measurement Errors for Lithium–Ion Batteries. *Batteries* **2024**, *10*, 368. <https://doi.org/10.3390/batteries10100368>

Academic Editor: Zhenzhen Wei

Received: 24 July 2024

Revised: 14 October 2024

Accepted: 14 October 2024

Published: 16 October 2024



Copyright: © 2024 by the author. Licensee MDPI, Basel, Switzerland. This article is an open access article distributed under the terms and conditions of the Creative Commons Attribution (CC BY) license (<https://creativecommons.org/licenses/by/4.0/>).

1. Introduction

Electrochemical batteries, such as lithium–ion (Li-Ion) batteries, are becoming increasingly used in several applications. Examples of these applications include, but are not limited to, Electric Vehicles and Hybrid Electric Vehicles (EVs and HEVs), power grid-scale energy storage, homes' and buildings' solar energy systems, aerospace systems, and the growing market of consumer portable electronic devices (e.g., tablets, smartphones, smartwatches, and fitness and health monitoring devices), among others [1–18].

Accurate and fast state-of-health (SOH) estimations or diagnoses and early fault detections are critical for the reliability and safety of both these batteries and the demanding applications they are being used in. In power-demanding applications, such as the EVs application, Li-Ion batteries can usually only be used down to a 70–80% SOH (or initial capacity) before they are replaced, due to increased failure and fire risks [19,20]. In other words, EV batteries are retired when they still have 70–80% of their initial capacity. When such batteries retire from their original power-demanding application, they can be used as second-use or second-life batteries in less demanding applications, such as in backup power for telecom and datacenter applications, behind-the-meter energy storage in residential or commercial applications, and front-of-the-meter storage for utility scale services that target applications for frequency regulation, voltage support, and excess renewable energy

storage [7–10]. For second-use/-life applications, the importance of accurate and fast SOH estimations increases due to the need for remaining life estimations with lower costs, the need to optimize the utilization of these second-use/-life batteries as a function of their degrading health to extend their life, and to reduce the potential early failure and fire risks [19–21].

The methods that are used to estimate the SOH of batteries can be divided into two main categories in terms of the required measurement time. Category #1 includes, but is not limited to, methods that require the information of the complete charging/discharging cycle of the battery (or a large portion of it), such as the direct capacity measurement method by Coulomb Counting, among others [4,5,11,22,23]. Category #2 includes methods that do not require the charging/discharging of the battery and instead utilize the impedance of the battery [6,24–27].

The direct capacity measurement method (the remaining capacity measurement) for SOH estimation is one of the most straightforward and most accurate methods if the battery's current is measured accurately to count the columns and if the measurements are performed under a controlled set of parameters, such as temperature. However, in order to measure the remaining capacity, at least one complete charge/discharge cycle or a predetermined large portion of the charge/discharge cycle is needed. Not only can this take hours (based on the capacity of the battery), but it also requires completing the charge and discharge cycle, which might not be possible/practical for online measurements and SOH estimations. Therefore, it is a slow method and a method that has better accuracy when used offline and in laboratory-controlled settings, even though it can be utilized for online estimations of the state of charge (SOC) and the SOH. This method is usually used to calibrate the accuracy of other methods, such as impedance-based methods.

Utilizing the EIS information for SOH estimation is drawing increasing attention due to its speed, in addition to its ability to reflect the internal changes to the battery. Measuring the EIS of a battery for a frequency range can be done in minutes or seconds, without the need to wait for a complete charge/discharge cycle (or large portion of it). As is the case for other methods, such as the direct capacity measurement method, the accuracy of SOH estimation based on information obtained from the EIS of a battery is highly dependent on the accuracy of the measurements. Measuring an accurate and consistent EIS across a frequency range is challenging and usually requires expensive equipment and the frequent calibration of the equipment. The small change in impedance values as a function of the SOH makes the needed measurement accuracy (especially when there is shift or offset in the measurements) even more challenging to achieve. Example algorithms that utilize information from the EIS of a battery include, but are not limited to, DC impedance (or the zero-phase impedance point), the EIS minimum impedance magnitude point, and the 1 kHz (or another frequency) impedance point, among others. Therefore, improving the accuracy of the EIS measurement is critical to achieving a fast and accurate EIS-based SOH estimation. Moreover, devising SOH indicators from the EIS of a battery that are less sensitive to measurement shift/offset or error is desired. This is the main objective of the research results presented in this article. Furthermore, in this work, the EIS was measured for a lithium-ion battery that was down to a ~15% SOH (i.e., deeply aged to a highly degraded condition), which was not only used to support the conclusions of this paper, but also helped fill a gap in the literature for EIS data under deep/high degradation levels.

2. Phase–Magnitude Relationship/Plot Principle

Commonly, researchers and designers utilize relationships/plots, such as Bode plots [28] and/or Nyquist plots [26,29], to study and analyze the characteristics of a device or system. This includes studying the Electrochemical Impedance Spectroscopy (EIS) [6,24–27] or, in other words, the frequency response of the electrochemical impedance of the electrochemical batteries.

Bode plot, as illustrated in the example of Figure 1, consists of two separate plots/graphs that show the magnitude (usually in decibels) on the y-axis of the plot/graph as a

function of frequency on the x-axis of the plot/graph and the phase on the y-axis of the plot/graph as a function of frequency on the x-axis of the plot/graph (expressing phase shift). For an EIS of a battery, Bode plot shows the values of the complex impedance magnitude ($Z_{mag} = Z_{mod}$ as given by Equation (1)) and phase ($\theta_Z = Theta_Z$ as given by Equation (1)), each as a function of frequency.

$$\begin{aligned} Z_{EIS} &= Z_{real} + jZ_{imag} = Z_{mag}\angle\theta_Z = Z_{mod}\angle Theta_Z \\ &= \sqrt{Z_{real}^2 + Z_{imag}^2} \angle(\tan^{-1} Z_{imag}/Z_{real}) \\ &= Z_{mag} \times [\cos\theta_Z + j\sin\theta_Z] \end{aligned} \quad (1)$$

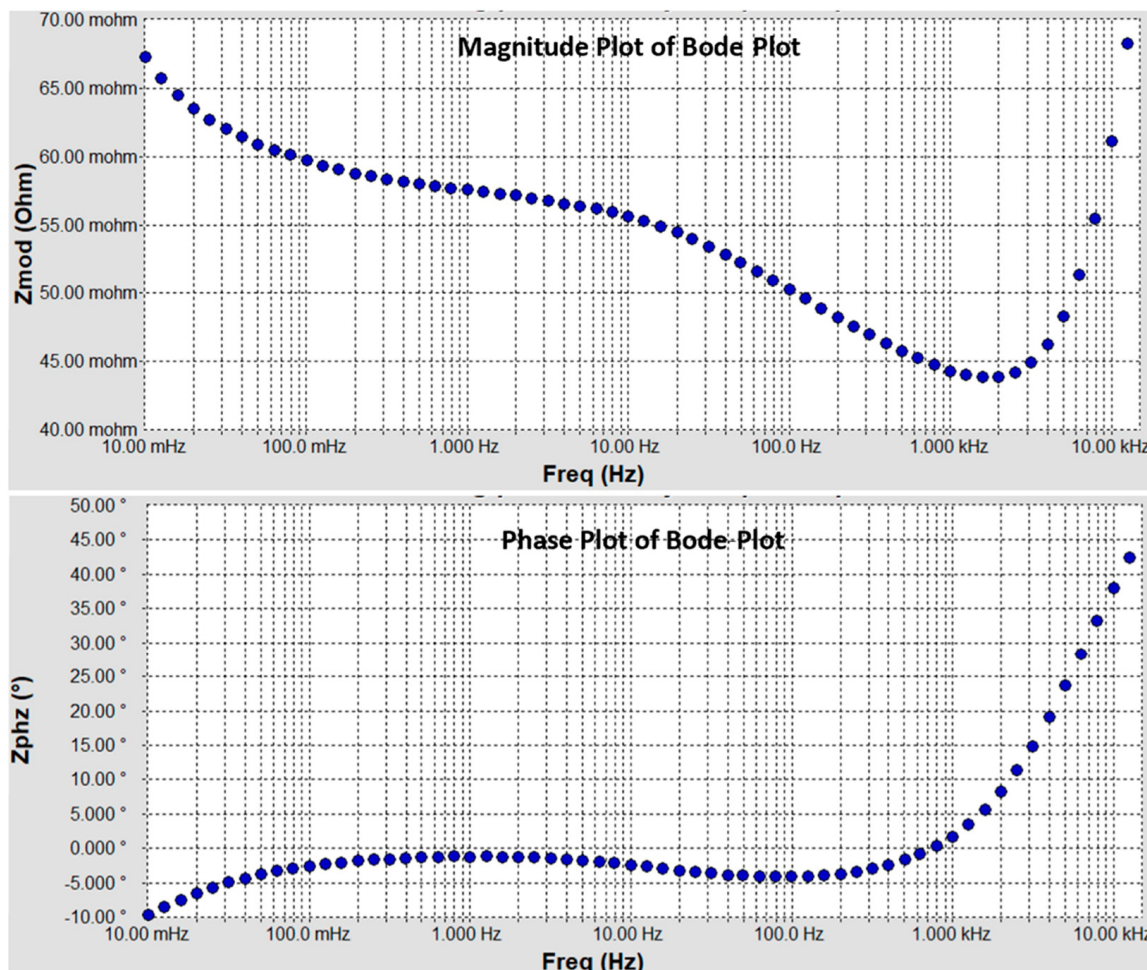


Figure 1. Bode plot (magnitude plot and phase plot as a function of frequency) for the values of the complex impedance (10 mHz–10 kHz) obtained from the measured EIS of a Tenergy ICR 18650-2600 Li-Ion battery cell [30] using the Gamry interface 5000E potentiostat [31].

Nyquist plots, as illustrated in the example of Figure 2, consist of a single plot/graph that shows the imaginary part of the complex number (or its negative) on the y-axis and the real part of the complex number on the x-axis. For an EIS of a battery, the Nyquist plot shows the negative of the imaginary part of the complex impedance ($-Z_{imag}$ as given by Equation (1)) and the real part of the complex impedance (Z_{real} as given by Equation (1)). Unlike the Bode plot, the Nyquist plot does not show the frequency information on one of its two axes, even though each point corresponds to a frequency point/value.

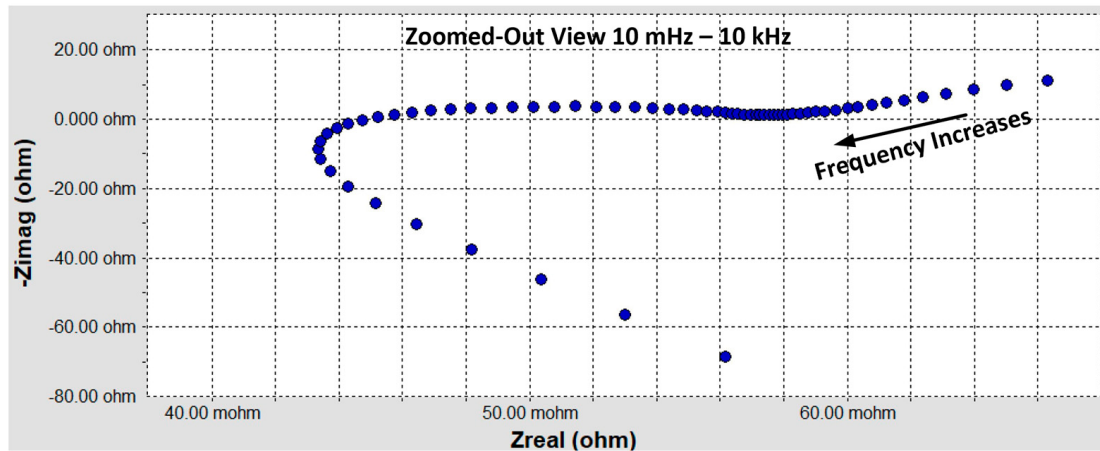


Figure 2. Nyquist Plot for the values of the complex impedance obtained from the measured EIS of a Tenergy ICR 18650-2600 Li-Ion battery cell [30] using the Gamry interface 5000E potentiostat [31].

Researchers have studied the Bode plots and Nyquist plots of batteries' EISs and have devised or utilized features from these plots that indicate the state of health (SOH) and the state of charge (SOC), among other characteristics [13,26,27]. In this section, a new relationship/plot is introduced which opens the door for new SOH-related features or indicators that were devised from the EISs of lithium-ion batteries. One of these features is discussed in the next section, and others are currently being investigated.

Figure 3 illustrates the presented Phase–Magnitude relationship/plot using the same EIS data that were used for the Bode plot of Figure 1 and the Nyquist plot of Figure 2. The EIS data are for a Tenergy ICR 18650-2600 lithium-ion battery cell [30] that was measured using the Gamry interface 5000E potentiostat [31]. As discussed in the next section, this relationship/plot exhibits features that are related to the SOH of Li-Ion batteries and has several advantages. Unlike the Bode plot, the presented Phase–Magnitude relationship/plot consists of a single two-dimensional plot with no frequency axis. Unlike the Nyquist plot, the presented Phase–Magnitude relationship/plot consists of a plot that shows the magnitude and phase information instead of real and complex components/parts.

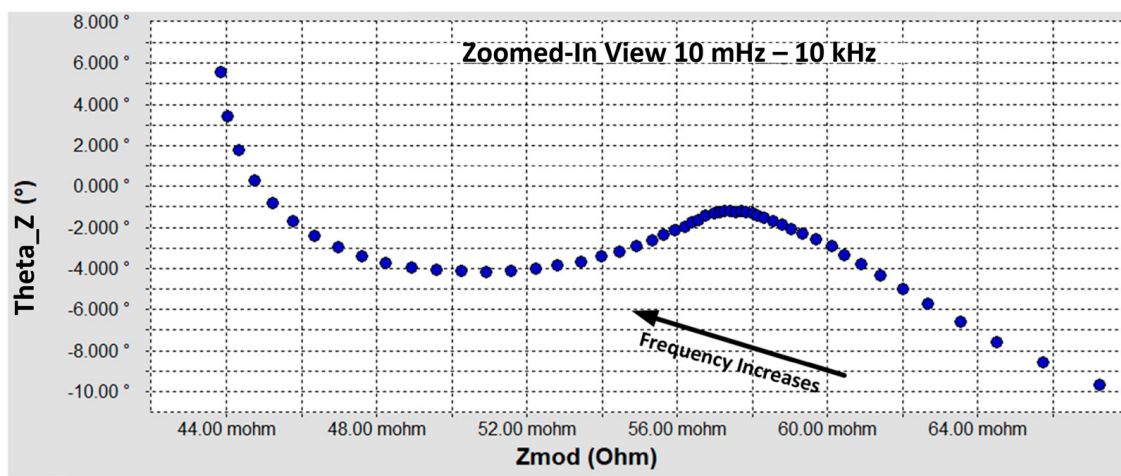


Figure 3. The presented Phase–Magnitude relationship/plot for the values of the complex impedance obtained from the measured EIS of a Tenergy ICR 18650-2600 Li-Ion battery cell [30] using the Gamry interface 5000E potentiostat [31].

3. Differential Impedance SOH Indicator Based on the Phase-Magnitude Relationship

A Tenergy ICR 18650-2600 Li-Ion battery cell [30] was aged by performing charge/discharge cycling at 2.6 A charge/discharge current (1 C rate). During each charging

operation, the Constant Current (CC) charging mode, at 2.6 A, was performed until the battery terminal voltage reached 4.2 V. Once this voltage was reached, the CC charging mode was terminated, and the Constant Voltage (CV) charging mode was initiated. The CV charging mode was terminated when the battery current reached 50 mA [32]. During the discharging mode phase, the battery cell was discharged with a 2.6 A current (1 C rate) until its terminal voltage reached 2.7 V. Before performing the measurements, such as the remaining capacity measurements and the EIS measurements, the battery was put into a rest state for 12 h to make sure it reached the thermal equilibrium state. In this work, the battery was aged down to a ~15% SOH (i.e., deeply aged to a highly degraded condition).

Figure 4 shows the Phase–Magnitude plots for the measured battery cell’s EIS as the number of ageing cycles increased and, therefore, as the battery cell aged (the SOH decreased). Figure 5 shows the capacity-based measured SOH value (which required at least one charge/discharge cycle over several hours to measure) for each EIS Phase–Magnitude plot (which required up to few minutes to measure), shown in Figure 4. The SOH value was calculated by using Equations (2) and (3).

$$SOH = \frac{Q_{available}}{Q_{nominal}} \times 100\% \quad (2)$$

$$Q_{available} = i_{discharge} \times (t_{full} - t_{empty}) \quad (3)$$

where SOH is the remaining capacity-based state of health, $Q_{nominal}$ is the nominal capacity of the battery (i.e., the amount of charges the battery can supply to a load or discharge before it reaches the minimum voltage) when it is new or not aged in a Coulomb unit, $Q_{available}$ is the actual available capacity or total amount of charges the battery can supply to a load (discharge) in a Coulomb (C) unit, $i_{discharge}$ is the constant discharge current used to measure $Q_{available}$ (2.6 A in this paper), t_{full} is the time instant (in seconds) at the beginning of the discharge operation when the battery cell is fully charged, and t_{empty} is the time instant when the battery voltage reaches the end of discharge voltage, which is 2.7 V in this paper.

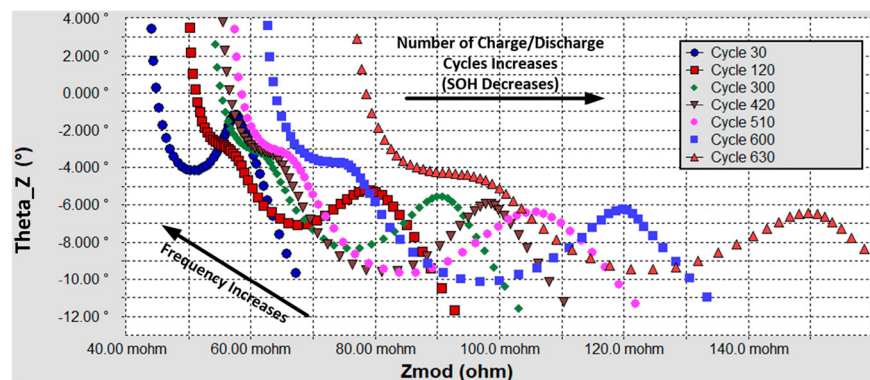


Figure 4. Experimentally measured Phase–Magnitude plots of the EIS as a function of ageing cycles (charge/discharge cycles) for a Tenergy ICR 18650-2600 Li-Ion battery cell [30] using the Gamry interface 5000E potentiostat [31].

One of the characteristics of the presented EIS Phase–Magnitude plot/relationship can be described as follows: as the frequency increases, starting from near zero, there is a first-phase peak (θ_{peak}) point followed by a last-phase valley (θ_{valley}) point (on the y-axis or phase axis). These two points are marked on Figure 5 for the sample EIS Phase–Magnitude curve, selected from Figure 4.

The $\Delta Z_{PM-Diff} = |Z_{phase-peak} - Z_{phase-valley}|$ mostly represents the charge transfer ability of the battery cell. The decrease in charge transfer [33] leads to the reduction of the battery’s effective capacity, i.e., the total amount of charges that can be released from the battery

to the load. In other words, when the battery cell's charge transfer ability decreases as it ages (when the SOH degrades), the value of $\Delta Z_{PM-Diff} = |Z_{phase-peak} - Z_{phase-valley}|$ increases.

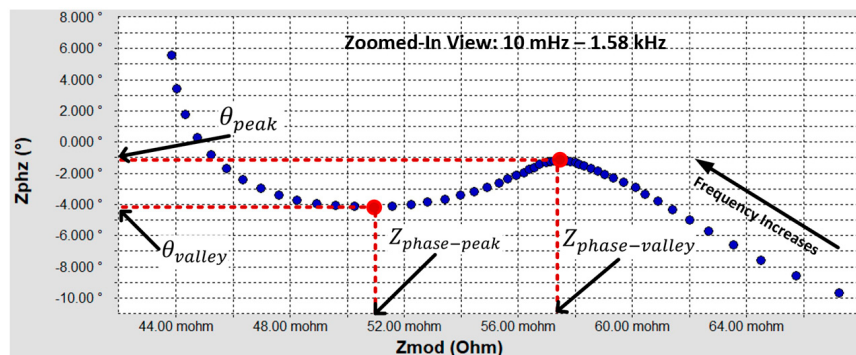


Figure 5. Selected curve from Figure 4 for Experimentally Measured Phase–Magnitude plots of EIS of Tenergy ICR 18650-2600 Li-Ion battery cell [30] marking selected data points of interest.

As can be seen from Figure 6, and as expected, the SOH decreases as the number of charge/discharge cycles that the battery goes through increases. There are several corresponding changes to the EIS Phase–Magnitude relationship/plot that can be observed from Figure 4 as the SOH decreases. One of the changes that can be strongly correlated to the SOH can be described as follows: as the battery's SOH decreases, the distance on the x-axis (impedance magnitude axis) between the first-phase peak point and the last-phase valley point increases.

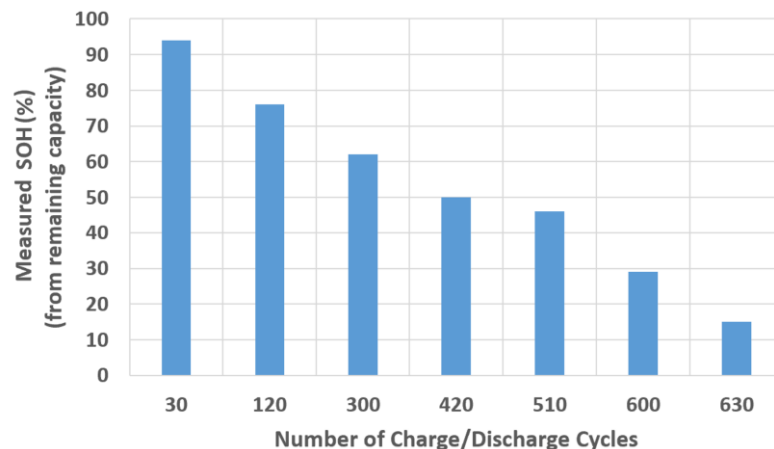


Figure 6. The percentage SOH of a Tenergy ICR 18650-2600 Li-Ion battery cell [30] as a function of the number of charge/discharge (ageing) cycles.

Based on the above, the phase-based differential impedance magnitude ($\Delta Z_{PM-Diff}$) of the first-phase peak point and last-phase valley point of the Phase–Magnitude relationship is defined as given by Equation (4), where $Z_{phase-peak}$ is the impedance magnitude value at the first-phase peak value (θ_{peak}), and $Z_{phase-valley}$ is the impedance magnitude value at the last-phase valley value (θ_{valley}). Figure 7 shows the SOH as a function of the phase-based differential impedance magnitude for the results shown in Figure 4 through Figure 6. The strong and consistent correlation between the SOH and the $\Delta Z_{PM-Diff}$ can clearly be observed.

$$\begin{aligned}\Delta Z_{PM-Diff} &= |Z_{phase-peak} - Z_{phase-valley}| \\ &= |(Z_{phase-peak} \pm Z_{offset}) - (Z_{phase-valley} \pm Z_{offset})|\end{aligned}\quad (4)$$

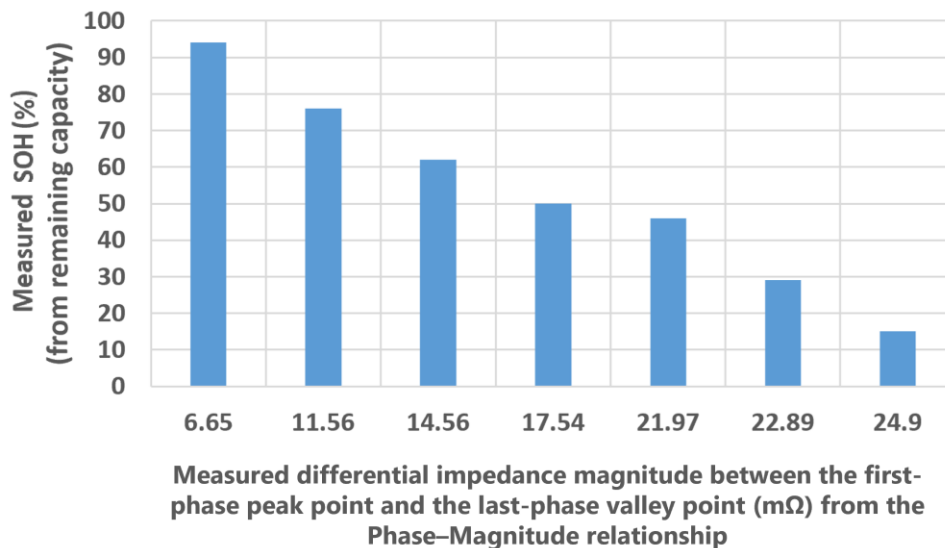


Figure 7. The percentage SOH as a function of the phase-based differential impedance magnitude of the first-phase peak point and the last-phase valley point of the Phase–Magnitude relationship for a Tenergy ICR 18650-2600 Li-Ion battery cell [30].

While there are also some correlations between the SOH and other individual points on the Phase–Magnitude relationship plot, such as the impedance magnitude at the first-phase peak point ($Z_{\text{phase-peak}}$ at θ_{peak}) by itself and the impedance magnitude at the last-phase valley point ($Z_{\text{phase-valley}}$ at θ_{valley}) by itself, the proposed phase-based differential impedance magnitude of the first-phase peak point and last-phase valley point $\Delta Z_{PM-Diff}$ (given by Equation (4)) has the following advantage: it has a higher immunity against the measurement shift/offset error (Z_{offset}) due to its differential nature and because the two impedance values ($Z_{\text{phase-peak}}$ and $Z_{\text{phase-valley}}$) are measured at a phase peak point (θ_{peak}) and valley phase point (θ_{valley}), regardless of the phase absolute values.

On the one hand, what is important in finding the $\Delta Z_{PM-Diff}$ value becomes the identification of the two points at which the phase peak and the valley occur, rather than the measurement accuracy of the phase values themselves at these two points. In real-time or during the $\Delta Z_{PM-Diff}$ tracking process, the occurrence of the phase peak can be detected when the phase or time shift between the battery's voltage and the battery's current is at a maximum (before it starts to decrease), and the occurrence of the phase valley can be detected when the phase or the time shift between the battery's voltage and the battery's current is at a minimum (before it starts to increase). On the other hand, what is important in finding the $\Delta Z_{PM-Diff}$ value becomes the difference between the impedance magnitude value at θ_{peak} ($Z_{\text{phase-peak}}$) and the impedance magnitude value at θ_{valley} ($Z_{\text{phase-valley}}$), as given by Equation (4), even if there is a shift/offset in the measurement of the impedance magnitude. In real-time or during the $\Delta Z_{PM-Diff}$ tracking process, the values of $Z_{\text{phase-peak}}$ and $Z_{\text{phase-valley}}$ can be obtained by dividing the battery's voltage magnitude by the battery's current magnitude at θ_{peak} and θ_{valley} , respectively, as given by Equation (5).

$$\begin{aligned} \Delta Z_{PM-Diff} &= |Z_{\text{phase-peak}} - Z_{\text{phase-valley}}| \\ &= \left| \frac{V_{\text{mag}}(\theta_{\text{peak}})}{I_{\text{mag}}(\theta_{\text{peak}})} - \frac{V_{\text{mag}}(\theta_{\text{valley}})}{I_{\text{mag}}(\theta_{\text{valley}})} \right| \end{aligned} \quad (5)$$

In order to obtain further validation for the presented $\Delta Z_{PM-Diff}$ SOH indicator, based on the presented Phase–Magnitude relationship/plot, the measured EIS data and the estimated capacity data for a Samsung 35E Li-Ion battery cell, as published by NASA researchers in reference [3], were utilized (for one battery cell example from this reference). Figure 8 shows the Phase–Magnitude plots for the measured battery cell's EIS as the number of ageing cycles increased and, therefore, as the battery cell aged (the SOH decreased),

while Figure 9 shows the SOH as a function of the phase-based differential impedance magnitude $\Delta Z_{PM-Diff}$.

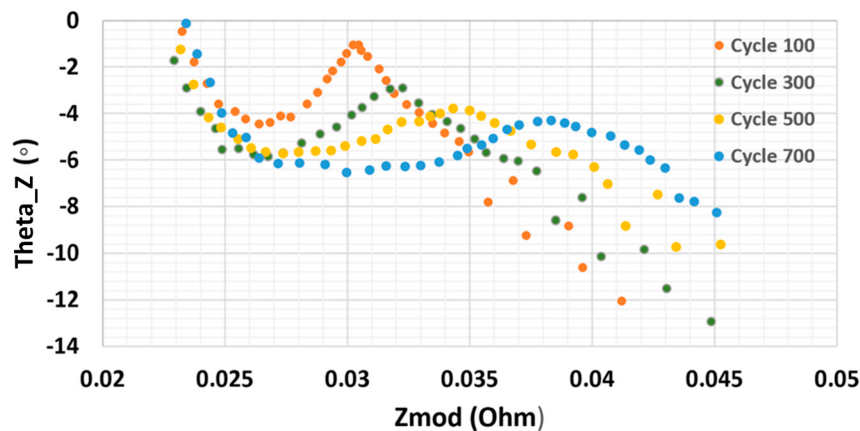


Figure 8. The experimentally measured Phase–Magnitude plots of the EIS as a function of ageing cycles (charge/discharge cycles) for a Samsung 35E Li-Ion battery cell, based on the data obtained by NASA, published in [3] (data points estimated from the Nyquist plots in [3]).

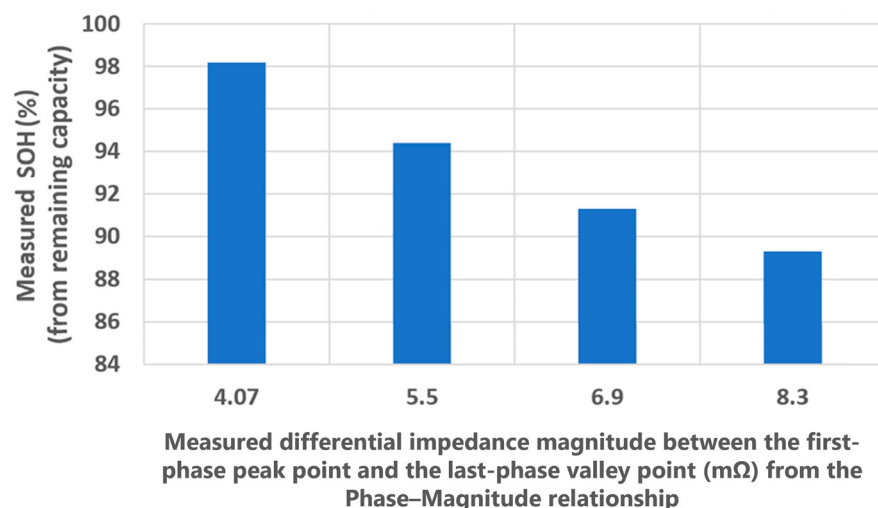


Figure 9. The estimated percentage SOH as a function of the phase-based differential impedance magnitude of the first-phase peak point and last-phase valley point of the Phase–Magnitude relationship for a Samsung 35E Li-Ion battery cell, based on the data obtained by NASA, published in [3] (data points estimated from the discharged capacity plot in [3]).

The results, based on the published data by the NASA researchers [3], for a Samsung 35E Li-Ion battery cell yielded the same conclusion (related to the strong relationship between $\Delta Z_{PM-Diff}$ and the SOH) as the one based on the data obtained by the author for the Tenergy ICR 18650-2600 Li-Ion battery cell. The following should be noted: (1) the EIS data were estimated from the Figure 6c Nyquist plot of reference [3], which is available down to only a ~89% SOH, and (2) the SOH values were estimated from the Figure 14 reference [3].

4. Additional Analysis and Observation

While the presented EIS Phase–Magnitude relationship and/or the phase-based differential impedance magnitude indicator of the SOH can be utilized in a variety of advanced algorithms (such as Machine Learning algorithms) for SOH estimation for improved SOH estimation accuracy, it can be observed from the results of the two battery cells in this paper that the relationship between the presented phase-based differential impedance

magnitude ($\Delta Z_{PM-Diff}$) of the EIS Phase–Magnitude relationship and the SOH can also be approximated with a relatively simple linear or polynomial function while maintaining a relatively good accuracy (especially when the SOH is higher than 50%). This can be used to provide an acceptable SOH estimation accuracy when simplicity/a low processing power is desired. However, such simplification might not be viable or sufficient in most cases, especially for batteries used in power-demanding applications and/or in variable and/or harsh environments, where, therefore, advanced algorithms would likely be needed.

Figures 10 and 11 show example linear and polynomial approximations for the relationship between $\Delta Z_{PM-Diff}$ and SOH, using the data obtained from the two battery cells (where y is the SOH and x is the value of $\Delta Z_{PM-Diff}$). The R-squared values are also shown for each approximation. It can be observed from Figures 10 and 11 that relatively high (close to 1) R-squared values can be obtained using a simple linear approximation (0.9529 for the Tenergy ICR 18650-2600 Li-Ion battery cell and 0.9831 for the Samsung 35E Li-Ion battery cell). By using higher order polynomial approximation, the R-squared values might be increased to be closer to one, as shown on the figures.

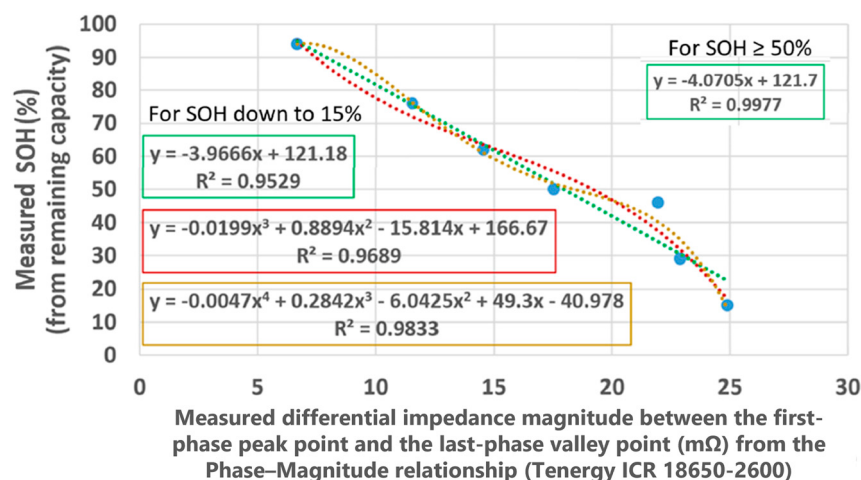


Figure 10. Linear and polynomial approximations and related R-squared values for the relationship between $\Delta Z_{PM-Diff}$ and the SOH using the data obtained from a Tenergy ICR 18650-2600 Li-Ion battery cell [30], where y is the SOH and x is the value of $\Delta Z_{PM-Diff}$.

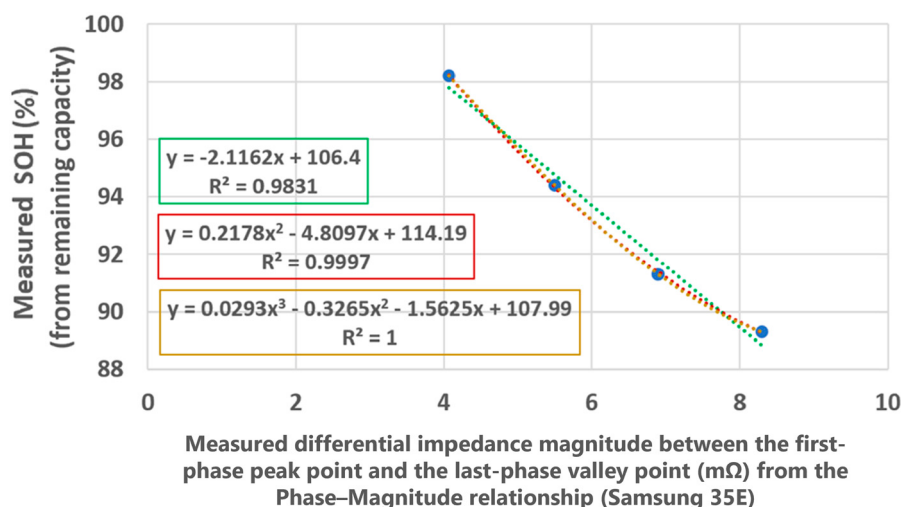


Figure 11. Linear and polynomial approximations and related R-squared values for the relationship between $\Delta Z_{PM-Diff}$ and SOH using the data obtained from Samsung 35E Li-Ion battery cell [3], where y is the SOH and x is the value of $\Delta Z_{PM-Diff}$.

The root mean square error (RMSE) values and the mean absolute percentage error (MAPE) values for both the batteries were calculated as summarized in Table 1 using Equation (6) and Equation (7), respectively.

$$RMSE = \sqrt{MSE} = \sqrt{\frac{1}{m} \sum_{i=1}^m (S_i - \tilde{S}_i)^2} \quad (6)$$

$$MAPE = \frac{100}{m} \sum_{i=1}^m \frac{|S_i - \tilde{S}_i|}{S_i} \quad (7)$$

Table 1. Calculated RMSE and MAPE values.

Battery	Polynomial Order	RMSE (%)	MAPE (%)
Tenergy	1 (down to 15% SOH)	5.4	12.4
Tenergy	3 (down to 15% SOH)	4.4	8.9
Tenergy	4 (down to 15% SOH)	4.8	12.6
Tenergy	1 (down to 50% SOH)	0.56	0.74
Samsung	1 (down to 89% SOH)	0.43	0.47
Samsung	2 (down to 89% SOH)	0.055	0.053
Samsung	3 (down to 89% SOH)	0.01	0.01

It can be observed that the RSME and the MAPE error values for the Tenergy ICR 18650-2600 Li-Ion battery cell are relatively small (<1%) when the approximation is performed using only the SOH values that are $\geq 50\%$, while they are not small when all the SOH values down to 15% are used in the approximation. From the results, it can be observed that this is because the relationship between the presented phase-based differential impedance magnitude ($\Delta Z_{PM-Diff}$) of the EIS Phase–Magnitude relationship and the SOH is almost linear for the SOH values that are $\geq 50\%$, while the relationship when the SOH values are <50% exhibit nonlinearity. For the Samsung 35E cell, the EIS data were available only down to a ~89% SOH, from reference [3], and as a result, the estimation error values are very small.

The data presented in this paper and used for SOH estimation were taken at a temperature of 25 °C. The characteristics and capacity of a lithium-ion battery changes as a function of temperature. Therefore, if a battery is not under a controlled temperature value, the SOH estimation models and algorithms need to take temperature variations into account [34,35].

5. Conclusions

The EIS of a Li-Ion battery can reveal significant and important information about the battery's performance, including those as it ages, such as the SOH. This work revealed that there is an EIS phase-based differential impedance magnitude value ($\Delta Z_{PM-Diff}$), based on an EIS Phase–Magnitude relationship, that has a strong and consistent correlation with the SOH of lithium-ion battery (or the remaining capacity). Therefore, $\Delta Z_{PM-Diff}$ can be used as an SOH indicator in SOH estimation algorithms. In addition, the $\Delta Z_{PM-Diff}$ -based SOH indicator has an additional advantage of reducing the effect of the shift/offset (error) in the EIS measurements on the SOH estimation's accuracy due to its differential nature. This is important because the accuracy of the SOH estimation is highly dependent on the accuracy of the measurements of the indicator used to indicate the SOH and on the strength and consistency of the correlation between the indicator and the SOH.

This article (a) introduced the principle of the SOH differential indicator, (b) presented battery aging data to validate the presented SOH differential indicator principle down to a low SOH value (deep ageing), (c) provided additional validation based on data from the literature, and (d) provided an illustration for how the presented SOH differential

indicator can be used for SOH estimation, based on a method which requires relatively low computational resources (as a first step towards future potential work on advanced and improved SOH algorithms that utilize the presented SOH differential indicator).

Future work includes, but is not limited to, deep ageing data collection from other types of batteries and at different temperature values; exploring other indicators from the EIS Phase–Magnitude relationship; the utilization of these indicators in SOH and SOC estimation algorithms, including, but not limited to, Machine Learning algorithms; accounting for the temperature effect on the capacity and the SOH; and SOH estimation.

Funding: This material is based upon work supported, in part, by the National Science Foundation (NSF, United States) under Grant No. 2213918. Any opinions, findings, and conclusions or recommendations expressed in this material are those of the author and do not necessarily reflect the views of the National Science Foundation.

Data Availability Statement: The original contributions presented in the study are included in the article, further inquiries can be directed to the author.

Conflicts of Interest: The author declares no conflicts of interest.

References

- Xiong, R.; Zhang, Y.; Wang, J.; He, H.; Peng, S.; Pecht, M. Lithium-Ion Battery Health Prognosis Based on a Real Battery Management System Used in Electric Vehicles. *IEEE Trans. Veh. Technol.* **2019**, *68*, 4110–4121. [[CrossRef](#)]
- Viswanathan, V.; Epstein, A.H.; Chiang, Y.M.; Takeuchi, E.; Bradley, M.; Langford, J.; Winter, M. The challenges and opportunities of battery-powered flight. *Nature* **2022**, *601*, 519–525. [[CrossRef](#)]
- Krause, F.C.; Ruiz, J.P.; Jones, S.C.; Brandon, E.J.; Darcy, E.C.; Iannello, C.J.; Bugga, R.V. Performance of commercial Li-Ion cells for future NASA missions and aerospace applications. *J. Electrochem. Soc.* **2021**, *168*, 040504. [[CrossRef](#)]
- Zou, B.; Xiong, M.; Wang, H.; Ding, W.; Jiang, P.; Hua, W.; Zhang, Y.; Zhang, L.; Wang, W.; Tan, R. A Deep Learning Approach for State-of-Health Estimation of Lithium-Ion Batteries Based on a Multi-Feature and Attention Mechanism Collaboration. *Batteries* **2023**, *9*, 329. [[CrossRef](#)]
- Liu, K.; Kang, L.; Xie, D. Online State of Health Estimation of Lithium-Ion Batteries Based on Charging Process and Long Short-Term Memory Recurrent Neural Network. *Batteries* **2023**, *9*, 94. [[CrossRef](#)]
- Cicioni, G.; De Angelis, A.; Janeiro, F.M.; Ramos, P.M.; Carbone, P. Battery Impedance Spectroscopy Embedded Measurement System. *Batteries* **2023**, *9*, 577. [[CrossRef](#)]
- Rallabandi, V.; Akeyo, O.M.; Jewell, N.; Ionel, D.M. Incorporating battery energy storage systems into multi-MW grid connected PV systems. *IEEE Trans. Ind. Appl.* **2019**, *55*, 638–647. [[CrossRef](#)]
- Chauhan, P.J.; Reddy, B.D.; Bhandari, S.; Panda, S.K. Battery energy storage for seamless transitions of wind generator in standalone micro-grid. *IEEE Trans. Ind. Appl.* **2019**, *55*, 69–77. [[CrossRef](#)]
- Ma, S.; Xin, D.; Jiang, Y.; Li, J.; Wu, Y.; Sha, G. Primary-Frequency-Regulation Coordination Control of Wind Power Inertia and Energy Storage Based on Compound Fuzzy Logic. *Batteries* **2023**, *9*, 564. [[CrossRef](#)]
- Masaud, T.M.; El-Saadany, E. Optimal battery planning for microgrid applications considering battery swapping and evolution of the SOH during lifecycle aging. *IEEE Syst. J.* **2023**, *17*, 4725–4736. [[CrossRef](#)]
- Xia, Z.; Abu Qahouq, J.A. Lithium-ion battery ageing behavior pattern characterization and state-of-health estimation using data-driven method. *IEEE Access* **2021**, *9*, 98287–98304. [[CrossRef](#)]
- Guo, W.; Sun, Z.; Vilnsen, S.B.; Meng, J.; Stroe, D. Review of “grey box” lifetime modeling for lithium-ion battery: Combining physics and data-driven methods. *J. Energy Storage* **2022**, *56*, 105992. [[CrossRef](#)]
- Xia, Z.; Abu Qahouq, J.A. State-of-charge balancing of lithium-ion batteries with state-of-health awareness capability. *IEEE Trans. Ind. Appl.* **2021**, *57*, 673–684. [[CrossRef](#)]
- Cheng, X.; Chen, X. Joint Concern over Battery Health and Thermal Degradation in the Cruise Control of Intelligently Connected Electric Vehicles Using a Model-Assisted DRL Approach. *Batteries* **2024**, *10*, 226. [[CrossRef](#)]
- Michelini, E.; Höschele, P.; Abbas, S.M.; Ellersdorfer, C.; Moser, J. Assessment of Health Indicators to Detect the Aging State of Commercial Second-Life Lithium-Ion Battery Cells through Basic Electrochemical Cycling. *Batteries* **2023**, *9*, 542. [[CrossRef](#)]
- Lin, G.; Liu, J.; Zhou, Y.; Li, Y.; Rehtanz, C.; Wang, S.; Wang, P.; Zuo, W. An inertia-emulation-based cooperative control strategy and parameters design for multi-parallel energy storage system in islanded DC microgrids. *IET Gener. Transm. Distrib.* **2022**, *16*, 4370. [[CrossRef](#)]
- Raoofi, T.; Yildiz, M. Comprehensive review of battery state estimation strategies using machine learning for battery Management Systems of Aircraft Propulsion Batteries. *J. Energy Storage* **2023**, *59*, 106486. [[CrossRef](#)]
- Sugumaran, G.; Prabha, N.A. A Comprehensive Review of Various Topologies and Control Techniques for DC-DC Converter-Based Lithium-Ion Battery Charge Equalization. *Int. Trans. Electr. Energy Syst.* **2023**, *2023*, 3648488. [[CrossRef](#)]

19. Cusenza, M.A.; Guarino, F.; Longo, S.; Ferraro, M.; Cellura, M. Energy and environmental benefits of circular economy strategies: The case study of reusing used batteries from electric vehicles. *J. Energy Storage* **2019**, *25*, 100845. [[CrossRef](#)]
20. Ahmadi, L.; Young, S.B.; Fowler, M.; Frazer, R.A.; Ahmadi, M. A cascaded life cycle: Reuse of electric vehicle lithium-ion battery packs in energy storage systems. *Int. J. Life Cycle Assess.* **2017**, *22*, 111–124. [[CrossRef](#)]
21. El Mejdoubi, A.; Chaoui, H.; Gualous, H.; Van Den Bossche, P.; Omar, N.; Van Mierlo, J. Lithium-ion batteries health prognosis considering aging conditions. *IEEE Trans. Power Electron.* **2019**, *34*, 6834–6844. [[CrossRef](#)]
22. Zheng, X.; Deng, X. State-of-health prediction for lithium-ion batteries with multiple gaussian process regression model. *IEEE Access* **2019**, *7*, 150383–150394. [[CrossRef](#)]
23. Park, K.; Choi, Y.; Choi, W.J.; Ryu, H.; Kim, H. LSTM-Based battery remaining useful life prediction with multi-channel charging profiles. *IEEE Access* **2020**, *8*, 20786–20798. [[CrossRef](#)]
24. Abu Qahouq, J.A.; Xia, Z. Single-perturbation-cycle online battery impedance spectrum measurement method with closed-loop control of power converter. *IEEE Trans. Ind. Electron.* **2017**, *64*, 7019–7029. [[CrossRef](#)]
25. Xia, Z.; Abu Qahouq, J.A. Ageing characterization data of lithium-ion battery with highly deteriorated state and wide range of state-of-health. *Data Brief.* **2022**, *40*, 107727. [[CrossRef](#)]
26. Huet, F. A review of impedance measurements for determination of the state-of-charge or state-of-health of secondary batteries. *J. Power Sources* **1998**, *70*, 59–69. [[CrossRef](#)]
27. Guha, A.; Patra, A. State of health estimation of Lithium-ion batteries using capacity fade and internal resistance growth models. *IEEE Trans. Transp. Electrif.* **2017**, *4*, 135–146. [[CrossRef](#)]
28. Wikipedia. Bode Plot. Available online: https://en.wikipedia.org/wiki/Bode_plot (accessed on 8 July 2023).
29. Wikipedia. Nyquist Stability Criterion. Available online: https://en.wikipedia.org/wiki/Nyquist_stability_criterion (accessed on 8 July 2023).
30. [Datasheet] Tenergy Corp., Fremont, CA, Tenergy Cylindric Lithium-Ion Cell 30005-0 Datasheet. Available online: <https://www.shorepowerinc.com/media/wysiwyg/files/Tenergy-30005-0-datasheet.pdf> (accessed on 8 July 2023).
31. Gamry Interface 5000E User Manual. Gamry Instruments Inc.: Warminster, PA, USA. Available online: <https://www.gamry.com/assets/Uploads/Interface5000-Users-Manual.pdf> (accessed on 8 July 2023).
32. Xia, Z.; Abu Qahouq, J.A.; Phillips, E.; Gentry, R. A simple and upgradable autonomous battery aging evaluation and test system with capacity fading and AC impedance spectroscopy measurement. *Proc. APEC* **2017**, 951–958. [[CrossRef](#)]
33. Gaberšček, M. Impedance spectroscopy of battery cells: Theory versus experiment. *Curr. Opin. Electrochem.* **2022**, *32*, 100917. [[CrossRef](#)]
34. Simatupang, D.; Benshatti, A.; Park, S.-Y. Battery Internal Temperature Measurement Using LC Resonant Tank for Battery Management Systems. *Batteries* **2023**, *9*, 104. [[CrossRef](#)]
35. Lin, X.; Perez, H.; Siegel, J.; Stefanopoulou, A.; Li, Y.; Anderson, R.D. Online Parameterization of Lumped Thermal Dynamics in Cylindrical Lithium Ion Batteries for Core Temperature Estimation and Health Monitoring. *IEEE Trans. Control Syst. Technol.* **2013**, *21*, 5. [[CrossRef](#)]

Disclaimer/Publisher's Note: The statements, opinions and data contained in all publications are solely those of the individual author(s) and contributor(s) and not of MDPI and/or the editor(s). MDPI and/or the editor(s) disclaim responsibility for any injury to people or property resulting from any ideas, methods, instructions or products referred to in the content.